

# Microstructural Effects on Damage Nucleation in Shock-Loaded Polycrystalline Copper



ANDREW DAVID BROWN, LEDA WAYNE, QUAN PHAM, KAPIL KRISHNAN, PEDRO PERALTA, SHENG-NIAN LUO, BRIAN M. PATTERSON, SCOTT GREENFIELD, DARRIN BYLER, KENNETH J. MCCLELLAN, AARON KOSKELO, ROB DICKERSON, and XIANGHUI XIAO

Polycrystalline copper samples with varying thermomechanical histories were shock loaded to induce spall *via* laser-driven plate impacts at low shock stress (<6 GPa). Electron backscattering diffraction was used to obtain statistics on grain boundary (GB) misorientations within the spall plane and at all GBs that contained damage. Specimens with pre-existing plastic deformation showed dominant intergranular damage at boundaries in the 25 to 50 deg misorientation range, while heat-treated samples had mixed trans- and intergranular damage with a lessened misorientation influence at damaged GBs. 3-D X-ray tomography data were used to analyze global volume statistics and qualitatively inspect the shape of voids present in samples of varying thermomechanical histories. It was found that annealed samples had a mixed mode of spherical- and sheet-like voids, indicative of trans- and intergranular damage, respectively, and the microstructure with the highest number of  $\Sigma 3$  twin boundaries had the highest concentration of spherical voids. Data from a plastically pre-strained sample showed a dominance of needle- and sheet-like voids, indicating primarily intergranular damage due to the higher strength of the bulk material forcing the damage to nucleate at weaker defects, in this case GBs.

DOI: 10.1007/s11661-014-2482-z

© The Minerals, Metals & Materials Society and ASM International 2014

## I. INTRODUCTION

**SHOCK** loading is a high stress, high strain rate phenomenon that occurs during high velocity impacts. Studying shock physics and material responses subjected to shock loading is of great importance in understanding dynamic events, such as ballistic impact, blast loading, space debris impact of space vehicles and satellites, automobile crash, geological events, *etc.* The predominant failure mode of metallic materials undergoing shock loading is spall failure. Spall failure may occur when the tensile release waves from the impact interact, causing a state of high tensile stress. If the state of stress at this interaction is greater than the strength of a ductile material, then there will be nucleation, growth, and coalescence of voids in the form of a spall plane.<sup>[1-3]</sup> The spall strength can be directly estimated from the velocity history of the target free surface over the time of the

impact. It has been shown that the microstructure of the material affects the local spall strength, since it provides preferential nucleation sites on and around the spall plane.<sup>[4,5]</sup> Specific variables in the microstructure known to affect the spall strength include anisotropy, grain size, intrinsic defects such as GBs and triple points, and extrinsic defects such as precipitates and inclusions.<sup>[1-12]</sup> The purpose of this work was to build upon the understanding of how local characteristics of the microstructure play a part in damage nucleation, which have not been fully addressed in the literature, particularly GB misorientation angle combined with thermomechanical history, by studying polycrystalline (PC) copper under shock loading with varying microstructures.

It is of interest to characterize adjacent grains with damage sites along the GB to elucidate what material characteristics at the microscale have the highest impact on localized damage nucleation in the microstructure. In Wayne *et al.*,<sup>[9]</sup> the authors analyze intergranular damage in their PC copper samples to obtain statistics on the strength of GBs, and report that the boundaries with the highest probability to contain spall damage were found to be in the 35 to 40 deg misorientation bin, and also found a tendency for damage at 60 deg boundaries to occur at the tips of terminated twins. However, these authors acknowledged that more work was needed to determine whether the intrinsic strength of the boundary or localized stress concentrations dominate in void nucleation. Escobedo *et al.*<sup>[10]</sup> claim that voids do not nucleate at special  $\Sigma 1$  and  $\Sigma 3$  boundaries, in agreement with the overall trends reported earlier by Wayne *et al.*,<sup>[9]</sup> except for the

---

ANDREW DAVID BROWN, Ph.D. Student, LEDA WAYNE, Graduate Student, QUAN PHAM, Undergraduate Student, KAPIL KRISHNAN, Postdoctoral Researcher, and PEDRO PERALTA, Professor, are with the Ira A. Fulton Schools of Engineering, Arizona State University, Tempe, AZ 85287. Contact e-mail: adbrown8@asu.edu SHENG-NIAN LUO, Director, is with the Peac Institute of Multiscale Sciences, Chengdu, P.R. China. BRIAN M. PATTERSON, SCOTT GREENFIELD, DARRIN BYLER, KENNETH J. MCCLELLAN, AARON KOSKELO, and ROB DICKERSON, Technical Staff Members, are with the Los Alamos National Laboratory, Los Alamos, NM 87545. XIANGHUI XIAO, Assistant Physicist, is with the Argonne National Laboratory, Argonne, IL 60439.

Manuscript submitted March 31, 2014.

Article published online August 15, 2014

exclusion of the tips of annealing twins (terminated twins), which are incoherent  $\Sigma 3$  boundaries, from being considered “weak.” Note that the experimental observations reported in References 8 and 9 of differences in spall damage nucleation between coherent and incoherent  $\Sigma 3$  boundaries are consistent with molecular dynamics modeling of their spall behavior.<sup>[13,14]</sup> More recently, Escobedo *et al.*<sup>[11]</sup> compared shocked copper and tantalum specimens of varying microstructures to determine where damage exists relative to the GBs. Results once again showed that low coincidence, high-angle GBs were preferred sites for damage, irrespective of grain size in copper, but dominant intergranular damage was found in tantalum. The work presented here aims to investigate the strength of GBs at the incipient stage of damage nucleation, with limited growth achieved from having shorter shock pulse durations than in previous work,<sup>[10]</sup> while achieving higher states of stress to allow for competition between inter- and transgranular damage nucleation. Samples of differing thermomechanical histories are investigated to study the effects of pre-existing plastic deformation which has on damage nucleation sites, something not done in previous works.<sup>[9-11]</sup> A careful statistical analysis, similar to those found in References 9, 12, and 15, is presented here for GBs with damage, taking into account the frequency of all GBs with and without damage to obtain a normalized, true probability for predicting damage at any given misorientation range.

Although 2-D studies are adequate for statistics on where damage is found within the microstructure, it is of interest to quantify the amount of inter- and transgranular damage present within a shock-loaded sample. Three-dimensional data are needed to characterize precisely where voids are located within the microstructure because with 2-D data, it cannot be determined if the damage studied is at the beginning, middle, or tail of any one void, making it impossible to know where it may have nucleated and which direction it grew. Three-dimensional characterization of shocked tantalum samples was performed in Reference 16, and even though the voids had not coalesced, they had an average diameter 4 times larger than that of the average grain size. The studies present in Escobedo *et al.*<sup>[10]</sup> analyze damage sites at GBs where the voids are approximately the same size as the surrounding microstructure, creating ambiguity when trying to discern the original nucleation site within the microstructure.

The aim of this work was to analyze 2-D statistics of GBs that contain damage and draw conclusions on how thermomechanical conditioning affects damage nucleation within the microstructure and support these conclusions with void shapes indicative of inter- or transgranular damage from 3-D XRT data.

## II. EXPERIMENTAL PROCEDURES

Laser-driven shock loading *via* flyer plates provides a method for studying incipient stages of spallation from a high strain rate ( $10^5$  to  $10^7$ ) shock experiment. Short pulse durations are required for ensuring incipient spall

conditions, and this was achieved *via* standard flyer-target impact tests conducted with a 2:1 ratio in target to flyer thickness along with a target diameter to thickness ratio of 10:1 to ensure mid-plane spallation and primarily one-dimensional conditions in the central portion of the target.<sup>[3]</sup>

All targets were prepared from a rolled plate of high-purity Hitachi copper (99.995 pct, half-hard, nominal cold reduction of 21 pct) with an average grain size of 150  $\mu\text{m}$ . They were polished within  $\pm 10$  pct of the desired 1 mm thickness and finished with 0.05  $\mu\text{m}$  colloidal silica while maintaining a parallel face tolerance of approximately 0.05 deg. The PC targets underwent heat treatment (HT) and full recrystallization (FR) processes at 473 K (200 °C) for 1 hour and 873 K (600 °C) for 1 hour under inert atmosphere, respectively, resulting in average grain sizes of 120 and 50  $\mu\text{m}$ , respectively. Targets that were tested without any heat treatment are labeled “as-received” (AR) and had an average grain size of 150  $\mu\text{m}$ . All flyer plates were harvested from (1 0 0) copper single crystals grown with a modified Bridgeman technique and polished to a thickness of 0.5 mm ( $\pm 10$  pct) using the same procedure as the targets.

Dynamic testing was conducted at the Trident laser facility at Los Alamos National Laboratory (LANL). Trident contains a Nd:glass laser that operates at a fundamental wavelength of 1054 nm and produces a homogenous drive for uniform acceleration of the flyer. Additional information on the drive beam setup can be found in Reference 8. The target sample rested flush against a 9.53-mm-thick PMMA (Plexiglass) window on the diagnostic side through which the velocity history could be recorded using point and line VISARs (Velocity Interferometry Systems for Any Reflectors). Standard hydrodynamic approximations<sup>[3,8,17]</sup> were used to account for the effects of the PMMA window on maximum shock stress ( $P_{\text{max}}$ ), the amplitude of tensile pulse reflected from the window ( $\sigma_{\text{refl}}$ ), spall stress ( $\sigma_{\text{spall}}$ ), and strain rate ( $\dot{\epsilon}$ ). The flyer was mounted to an assembly with a sapphire substrate and rested against a confinement layer made of a Cu disk (0.1 to 0.5 mm thick). Testing conditions were such that tensile shock stresses were at and slightly above the spall strength of the targets to ensure incipient spall conditions with minimal to moderate void growth. The target specimens chosen for this study possess clear spall signatures from their VISAR records. Table I shows the testing conditions for the analyzed specimens. Sample 7 was chosen because it had a higher maximum shock stress ( $P_{\text{max}}$ ) associated with it, which should lead to insight on the competition between inter- and transgranular damage nucleation, along with comparing statistics of GB strength between two annealed samples with different stress states. Samples 6 and 7 also have the largest fraction of strong  $\Sigma 3$  boundaries, allowing for the study of how these boundaries potentially mitigate the overall probability for damage nucleation at GBs.

The targets were examined using optical microscopy, scanning electron microscopy (SEM), Electron back-scattering diffraction (EBSD), and 3-D XRT to characterize the spall damage and surrounding microstructure.

**Table I. Shock Conditions for Cu PC Experiments**

Shot ID# & Microstructure	Flyer Velocity (m/s)	$P_{\max}$ (GPa)	$\sigma_{\text{spall}}$ (GPa)	Av. Grain Size ( $\mu\text{m}$ )
1/AR	169	3.07	1.48	150
2/AR	145	2.62	1.49	150
3/AR	148	2.67	1.46	150
4/AR*	205	4.11	1.22	150
5/FR	151	2.98	1.39	50
6/HT*	155	3.06	1.56	120
7/HT	250	5.04	1.82	120

The maximum shock stress and spall strength ( $\sigma_{\text{spall}}$ ) were obtained directly from the VISAR records.

\*Indicated sample only used for XRT studies.

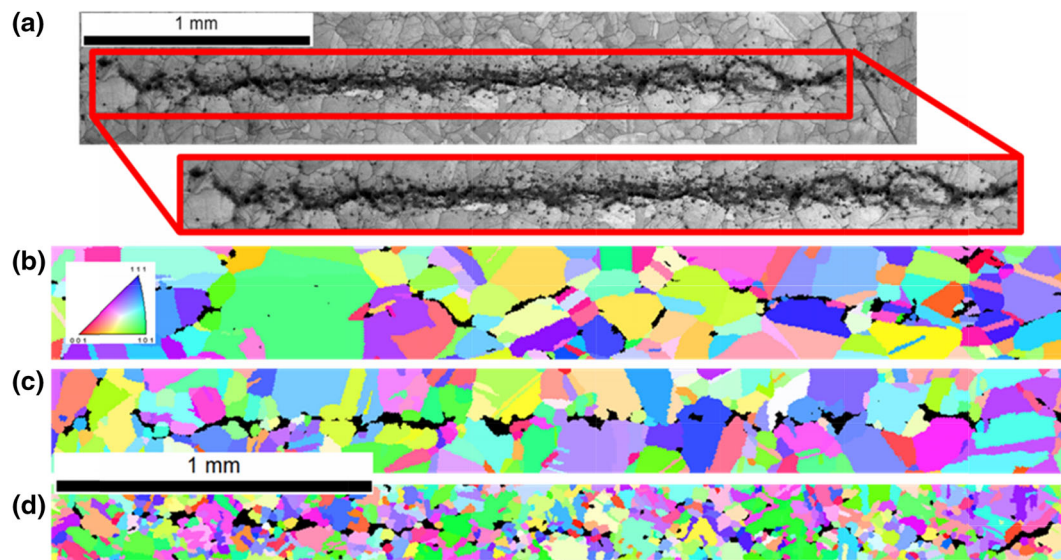


Fig. 1—(a) Selecting the spall zone from an image quality map in the EBSD software for GB distributions indicated by the red rectangle. This is a section taken from the HT sample 7. Inverse Pole Figure (IPF) maps from EBSD data are shown for (b) sample 1 (AR), (c) sample 7 (HT), and (d) sample 5 (FR). The black regions are voids.

Each specimen was sectioned in half using a diamond wheel before undergoing post-shot characterization. The post-shot analysis for this study involved consecutive cross sectioning the samples *via* mechanical polishing to gather 2-D statistics for GBs that contained damage. Material was removed between each analyzed section greater than or equal to the average grain size for each specimen to prevent double counting GBs for statistics. The AR specimens presented here for 2-D statistics were previously analyzed by Wayne *et al.*<sup>[9]</sup>.

It is important to consistently define the region of interest for taking statistics. In this case, the spall zone was taken by cropping the cross sections to encompass a rectangular area bounded by the upper- and lowermost voids across the entire damaged area. Previously reported data<sup>[9,11]</sup> from 2-D GB statistics did not take into account every GB within the spall zone. This results in an underestimation of the total number of GBs present, which, in turn, can lead to overprediction of the probability of finding damage given a misorientation angle. The work presented here accounts for all GBs

present in a spall zone defined by the cropping process described above, as illustrated in Figure 1, along with EBSD maps for all three microstructures studied in this work.

The presence of pre-existing plastic deformation in the AR specimens from their half-hard (nominal cold reduction of 21 pct) conditions, containing approximately 4 deg average orientation spread across grains, was handled by assigning an average orientation to each grain. The GBs with misorientations of 5 deg or less were not considered because a tolerance of 5 deg was used by the EBSD software to define a GB, which was applied for all specimens. Counts of angles were grouped into bins of 5 deg for each microstructure, ranging from 0 to 65 deg, and plotted on a histogram, with a horizontal error of  $\pm 5$  deg. As previously discussed in the literature,<sup>[9,12]</sup> it is important to normalize statistical distributions to estimate the frequency of damaged boundaries for a given misorientation as a fraction of the total boundaries for each misorientation bin within the area of interest. Bayes' theorem<sup>[11]</sup> was

implemented to normalize the damage distribution to find the true probability of finding damage ( $X = 1$ ) at a given GB given its misorientation angle  $\theta$ :

$$P(X = 1|\theta) = \frac{P(\theta|X = 1) \times P(X = 1)}{P(\theta)}. \quad [1]$$

$P(X = 1|\theta)$  is of interest because it takes into account the texture of the microstructure, whereas  $P(\theta|X = 1)$  is measured directly from binning all boundaries with damage and dividing each bin by the total number of damaged boundaries, artificially inflating the probability of finding damage for a misorientation range.  $P(X = 1)$  is the total number of damaged boundaries over the total number of boundaries, and  $P(\theta)$  is simply the total misorientation angle distribution. Vertical error bars were added to the distribution of  $P(X = 1|\theta)$  in order to elucidate if changes in probability between bins are relevant. The error bars were created by splitting the  $P(\theta|X = 1)$  and  $P(\theta)$  distributions into two sections, 0 to 50 deg and 50 to 65 deg, and fitting each section with a Johnson Sb distribution.<sup>[18]</sup> This is a highly flexible bounded distribution with two shape parameters and a scaling factor. For each microstructure, the Johnson Sb distributions were assigned random numbers equal to the number of damaged boundaries within that distribution's misorientation range and repeated 10,000 times. A standard deviation was found for the resulting number of counts in each 5 deg misorientation bin, and propagation of error<sup>[19]</sup> was applied to Eq. [1] to find the total error for  $P(X = 1|\theta)$ . The  $P(X = 1|\theta)$  distribution was compared to 3-D shape fitting data obtained from XRT to determine if thermomechanical histories affect where damage nucleates within the microstructure.

Rectangular sections with a  $1 \times 1 \text{ mm}^2$  cross section were exhumed from the central spall region of samples 4, 5, and 6 for 3-D XRT analysis. This provides for a comparison in the shapes of the voids from all three microstructures studied in the statistical analysis. Radiographs were taken of Samples 4, 5, and 7 at LANL; however, it was discovered that the damage present in the section scanned from sample 7 was toward the outer edge of the spall zone which may be affected by lateral release waves due to the geometry of the experiment, rendering the data unreliable for quantitative analysis. Information on the X-ray source and beam conditions at LANL may be found in Reference 20. X-ray tomography (XRT) data for sample 6 were collected at the Advanced Photon Source (APS) at the Argonne National Laboratory (ANL) on beam-line 2-BM. An uncollimated white beam with energy of 60 keV measuring  $50 \times 3 \text{ mm}^2$  (horizontal  $\times$  vertical) at the sample was used for data acquisition. The X-ray source was passed through 15 mm of glass and 15 mm of silicon to reduce beam hardening. The sample was rotated at 1.2 deg per second during acquisition, remaining within the full  $1.66 \times 1.4 \text{ mm}^2$  ( $2560 \times 2160$  pixels) field of view of the CCD camera.

All data sets underwent smoothing, segmentation, and thresholding procedures using the software package Avizo™ in order to remove artifacts, such as two separate voids appearing as one due to close proximity.

It has been reported that one needs  $\sim 80$  voxels in order to correctly measure the surface area of an object, where a voxel is a cube with sides equal to that of the pixel resolution of the data,  $\sim 120$  for the volume, and  $\sim 1000$  for the 3D Feret shape to maintain 10 pct or less absolute error.<sup>[20]</sup> The 3D Feret shape is a number used to quantify the relationship between the minimum and maximum feature lengths in an object; as this number approaches 1, the object becomes spherical. For samples 4 and 5 (AR and FR), the pixel size is  $2.24 \mu\text{m}$ , meaning one voxel is  $11.24 \mu\text{m}^3$  which requires a minimum volume of  $1124 \mu\text{m}^3$  for accurate 3D Feret shape measurements. Sample 6 (HT) has a pixel size of  $0.65 \mu\text{m}$ , making one voxel  $0.275 \mu\text{m}^3$ , corresponding to a minimum volume of  $275 \mu\text{m}^3$ . For the purpose of this work, it is important not only to capture the shape of voids for visual inspection, but also to maximize the number of voids analyzed for volume statistics. A series of volumetric sieves was performed at 500, 1000, 4000, and  $10,000 \mu\text{m}^3$  for samples 4 and 5 to visualize how much information is lost as the minimum volume for a void is chosen. This process is shown for sample 5 in Figure 2. For samples 4 and 5, the void minimum  $4000 \mu\text{m}^3$  sieve (corresponding void radius of  $\sim 10 \mu\text{m}$ ) was chosen for visual inspection of void shapes in this paper since it is well over the 120 voxel resolution for accurate volume resolution while preserving about half of the voids in the data set. A minimum volume of  $1000 \mu\text{m}^3$  was chosen for global statistics such as average void volume and void volume fraction because the shape is not of interest, but preserving the surface area and void volume is necessary. Due to the better resolution obtained from the APS data, sample 6 has a minimum void radius of  $\sim 4 \mu\text{m}$  with the 1000 voxel minimum; thus, its sieve was conducted at  $275 \mu\text{m}^3$  and used for both shape inspection and global statistics.

A strong distribution of spherical voids is indicative of transgranular damage, as voids tend to open as octahedrons in single crystals.<sup>[21]</sup> “Needle” and “sheet-like” voids are indicative of intergranular damage and/or coalescence. The more a void resembles a sheet/disk, the more likely that void is following a GB through the thickness of the material.

### III. RESULTS AND DISCUSSION

Consecutive cross sectioning revealed that the voids were predominantly intergranular for the AR specimens, whereas the HT and FR specimens contained a mixed mode of inter- and transgranular voids. This observation of inter- vs transgranular damage modes for the specimens presented here is supported by 3-D XRT reconstructions of each microstructure, as shown by Brown *et al.*<sup>[12]</sup> Examining the cross sections also shows that the damage had grown to sizes less than or equal to the grain size of each specimen, making it easier to decipher voids along GBs and at triple junctions for misorientation statistics. The total number of cross sections, total number of GBs in the spall plane, and the total number of damaged boundaries for each microstructure are AR: 27, 50,438, and 1164, HT: 10, 8446,

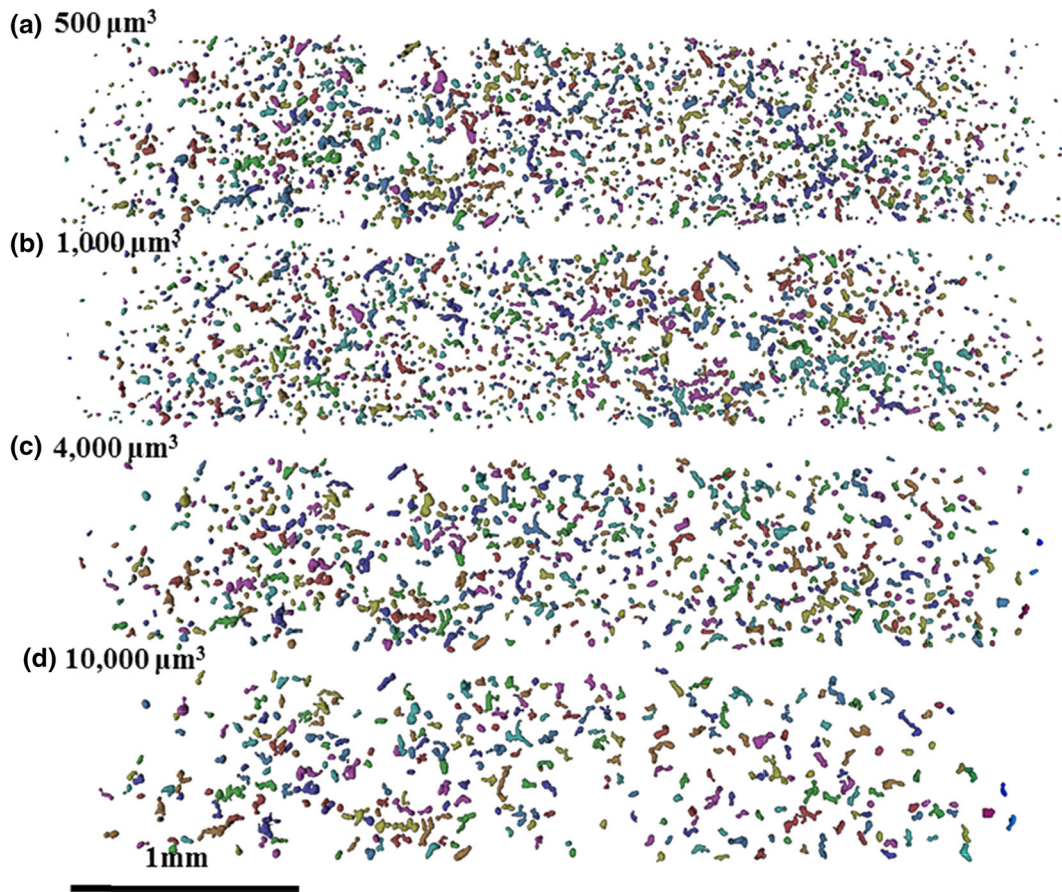


Fig. 2—Volumetric sieving process for sample 5 (FR). The minimum volume voids shown are (a) 1553 voids at  $500 \mu\text{m}^3$ , (b) 1260 voids at  $1000 \mu\text{m}^3$ , (c) 643 voids at  $4000 \mu\text{m}^3$ , and (d) 296 voids at  $10,000 \mu\text{m}^3$ . Void colors are random and for visual aid only.

and 556, and FR: 6, 25,749, and 827. The AR specimens contained spall that was more incipient, and had the largest grain size, of all three microstructures; thus, more sections were required to gather damaged GB statistics. Results show a strong GB texture toward the  $60^\circ$  range for all specimens, many of which are  $\Sigma 3$  twins, and peaks in damaged boundaries in the 30 to 50 deg range, with the largest peaks for the HT and FR microstructures again coming in the 60 deg range, as seen by plotting  $P(X=1|\theta)$  and  $P(\theta)$  in Figures 3(a) and (b), respectively.

Figure 4(b) shows an abundance of 60 deg misorientations containing damage, going against the now common wisdom that  $\Sigma 3$  boundaries are strong due to their low energy.<sup>[17]</sup> Some of the boundaries in the 60 deg range will be random high-angle GBs, making it important to find the total fraction of CSL boundaries for each sample. Figure 4 shows that there is significant texture toward  $\{111\} \Sigma 3$  and  $\{110\} \Sigma 9$ s, the latter appearing at junctions containing two  $\Sigma 3$ s.<sup>[22]</sup> The  $\Sigma 3$  fraction of boundaries for the HT, FR, and AR microstructures were found to be 0.536, 0.461, and 0.355, respectively, and the  $\Sigma 9$  fraction to be 0.052, 0.072, and 0.008, respectively, compared to  $\sim 0.7$  total fraction of  $\Sigma 3$  and  $\Sigma 9$  reported in Reference 10. This reduction in texture allows for more statistics to be gathered from the random high-angle GBs to be

compared to these well-documented special GBs. Removal of  $\Sigma 3$  boundaries from analysis pushes the density of all boundaries to follow the standard McKenzie distribution.<sup>[23]</sup>

After performing the normalization described in Eq. [1] and applying vertical error bars, the results shown in Figure 5 indicate that the overall shape of the histograms peak around the 30 to 35 deg range in the HT and FR specimens, but other modal peaks between bins are suspect; however, the general trend even with the presence of the error bars indicates a preference to the 25 to 50 deg range. The AR specimens have less error and possess a very pronounced peak between the 25 to 50 deg range, implying that these boundaries are microstructurally weaker than others, in full agreement with the qualitative conclusions offered in Reference 9. The magnitude of the probabilities to find damage in the HT microstructure is approximately doubled across every bin when compared to the FR and AR microstructures. Recall that the HT sample had the highest  $P_{\text{max}}$  of all tested samples, so this increase in global damage probability makes sense, though it appears to have little influence on the shape of the curve in Figure 5 when comparing with the fellow annealed FR sample.

The removal of plastic deformation in the grains via heat treatments creates less of a preference toward intergranular void nucleation, and the results from

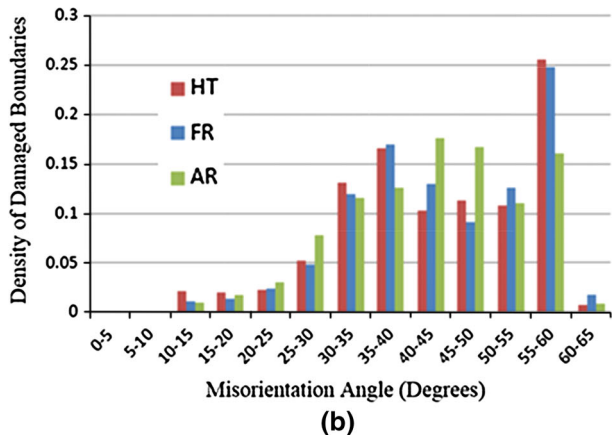
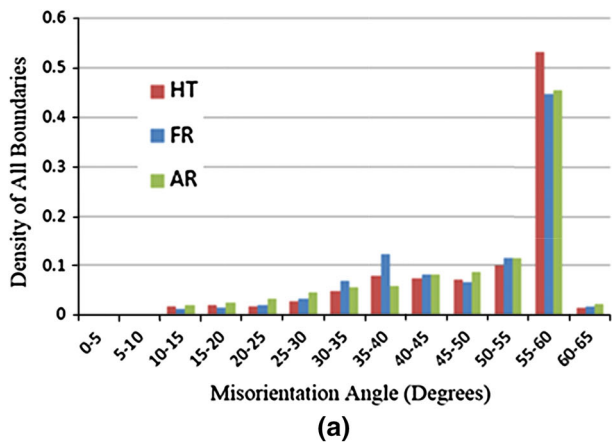


Fig. 3—2-D damage statistics for each microstructure: (a) all boundaries within the spall zone,  $P(\theta)$ ; (b) all damaged boundaries,  $P(\theta|X = 1)$ . There is a horizontal error of  $\pm 5$  deg for all data.

Figure 5 indicate that misorientation angle also has decreased influence on GB damage. These observations strongly suggest that when heat-treated copper PCs are subjected to shock loading, there is a tendency to find damage along the spall plane with less regard of the local microstructure as compared to the pre-strained specimens, with the possible exception of  $\Sigma 3$  twin boundaries, in agreement with.<sup>[9,10]</sup> Damage was found along some twin boundaries and, more commonly, at the tips of twins, which are likely not  $\{111\}$ , resulting in a higher energy boundary.<sup>[17]</sup> Copper PCs with plastic deformation have strain-hardened grains that effectively force void nucleation to the weaker defects in the material, in this case GBs. When damage is primarily intergranular, the local microstructure has a more pronounced effect on where damage is present based on the strength of the boundaries. The AR microstructure has the lowest number fraction of  $\Sigma 3$  and  $\Sigma 9$  boundaries, but also contains the lowest density of damaged boundaries in the  $\Sigma 3$  and  $\Sigma 9$  misorientation ranges, further supporting these findings. Random, high-angle GBs with misorientations of 25 to 50 deg range were found to be the weak links in all specimens, particularly in the AR samples, while low-angle GBs remain resilient to the presence of damage. Regarding  $\Sigma 3$  boundaries, they are also strong in a statistical

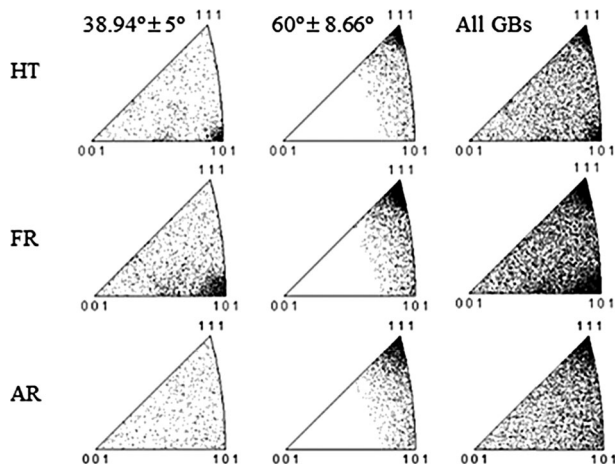


Fig. 4—Inverse Pole Figure (IPF) plots of the axis/angle misorientations for 3 random sections from each microstructure, corresponding to (from left to right):  $\Sigma 9$  range,  $\Sigma 3$  range, and all boundaries. The  $\Sigma 9$  and  $\Sigma 3$  misorientation ranges are from Bradon's criterion.<sup>[24]</sup>

sense, *i.e.*, they had one of the highest fractions of damaged GBs for all microstructures (Figure 4(b)); however, the number of damaged  $\Sigma 3$  GBs is only a small fraction of the total number of  $\Sigma 3$  GBs present in the cross-sectional area. In order to confirm that the AR specimens' dominant damage mode is intergranular and the annealed samples show little preference to where the voids nucleate, 3-D data sets from XRT were analyzed.

After going through smoothing, segmentation, and thresholding procedures, void volume statistics were analyzed from the 3-D XRT data. Table II shows these volumetric data for each sample. Note that the total volume fraction listed in Table II is the only entity that includes voids that share nodes with the perimeter of the dataset in order to correctly account for all voids that meet the 1000 and  $275 \mu\text{m}^3$  minimums for accurate volume rendering for samples 4 and 5, and 6, respectively. Voids that share faces or nodes with the edges, even if they were  $4000 \mu\text{m}^3$  or larger in volume, were not part of the void shape inspection as they are geometrically incomplete.

The voids in the HT specimen are the smallest of the three samples and appear to be the most incipiently spalled, as the total volume fraction of voids is also the lowest for the area analyzed. The voids present in the AR are the largest for both by average radius and volume despite having the least number of voids sampled, which leads to the hypothesis that the voids in this sample either (a) have begun to coalesce, or (b) nucleated and grew at intrinsically weak spots within the microstructure, *i.e.*, GBs. If (a) is the case, then one would expect to see a large fraction of oblong, needle-like voids, which would be the resulting shape when multiple spherical objects coalesce; and, if (b) is the case, then one would expect to see a large fraction of disk, or sheet-like voids present in the sample, indicative of intergranular damage following the GBs. Figure 6 shows a top-down view (shock direction is out of the page) of the voids in each sample.

In Figure 6, one can see a drastic difference in void shape distribution for all three cases. Qualitatively, we

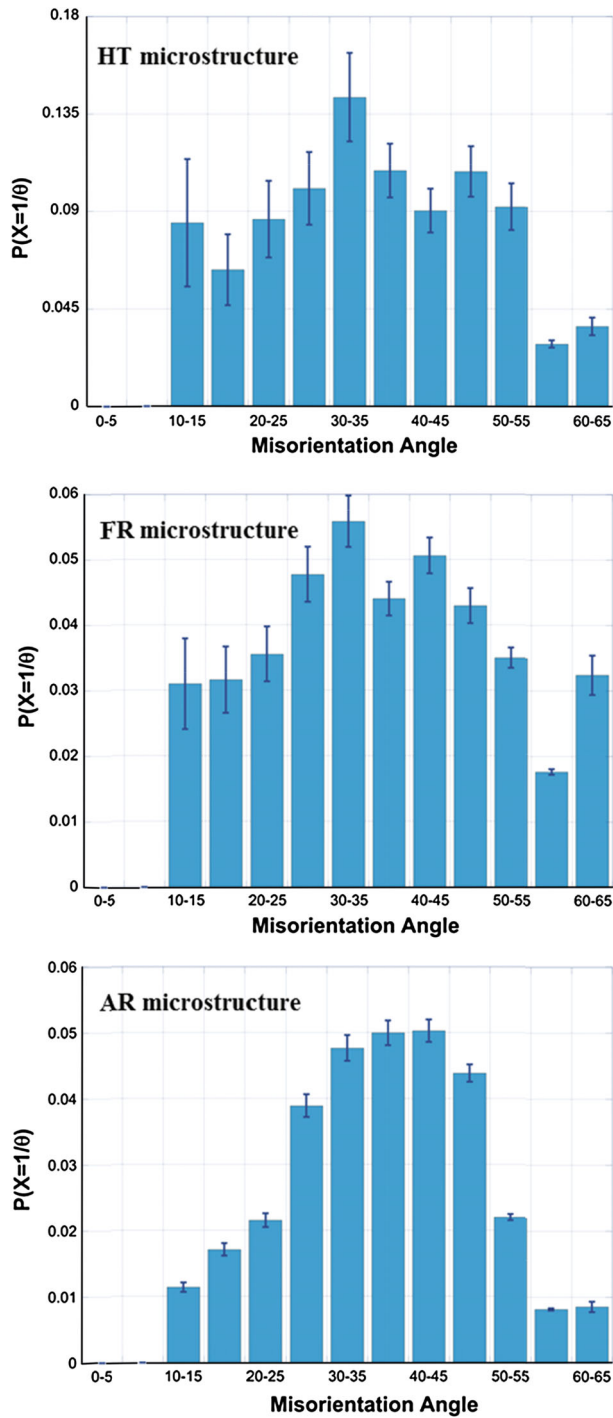


Fig. 5—Probabilities of finding a misorientation angle  $\theta$  with damage.

can tell that the AR sample in Figure 6(a) has a high concentration of needle to disk-shaped voids, which is indicative of void coalescence and intergranular damage. Upon visual inspection of the spall plane in both 2-D and 3-D, one can clearly see the voids along GBs and having curvature that would follow GBs. The needle-shaped density can come from coalescence, but also from damage along triple junctions. Figure 7(b) shows a zoomed in view of a few intergranular damage sites in the AR

**Table II. Volumetric Void Data Obtained From 3-D XRT With a Minimum Volume of  $1000 \mu\text{m}^3$  for Samples 4 and 5 and  $275 \mu\text{m}^3$  for Sample 6**

Sample #/Microstructure	4/AR	5/FR	6/HT*
Number of Voids	449	1260	669
Av. Vol. ( $\mu\text{m}^3$ )	12,034	8393	2450
Median Vol. ( $\mu\text{m}^3$ )	4031	4177	860
Av. Radius ( $\mu\text{m}$ )	11.7	11.04	6.89
Spall Zone Vol. ( $\mu\text{m}^3$ )	$1.09 \times 10^9$	$793 \times 10^6$	$237 \times 10^6$
Tot. Vol. Fraction	0.0116	0.0163	0.0069

\*Indicated sample only used for XRT studies.

sample. In Figure 6(b), there is a larger spread of void shapes for the FR microstructure; however, they are predominantly needle-shaped and spherical-shaped voids with very few sheet-like voids, indicative of transgranular damage and coalescence. Reviewing the 2-D and 3-D data sets, there is an apparent mixed mode of inter- and transgranular damage, but this microstructure has an average grain size that is approximately double the average void size, which results in less clear definition between intergranular damage vs damage that happens to be present at a boundary. Figure 6(c) shows there is a heavy skew toward spherical-shaped voids in the HT sample, matching 2-D SEM and EBSD data, which shows heavy transgranular damage. It is clear that the annealed samples 5 and 6 lean toward voids that resemble spheres and oblate and prolate ellipsoids. Figure 7(a) shows a zoomed in view of a region of coalesced voids in the HT sample, where the individual spherical-shaped voids in the clusters can still be distinguished. From the 2-D SEM and EBSD images, it was clear that there were many voids near GBs that appeared to be spherical. This supports the claim that the removal of plastic pre-strain *via* annealing actually diminishes the effect of the microstructure that has on preferential damage nucleation sites. For completeness, please be aware that a spherical void does not necessarily have to open transgranularly, and may open beside or even at a GB, but goes not grow or coalesce with other voids along the GB, which would make it appear to be disk shaped. It is proposed here that GBs that contain disk-shaped voids are weaker than GBs that contain damage that is spherical within a given microstructure, as the voids continued to grow along the GB. When comparing samples with different microstructures, there is strong evidence that plastic pre-strain encourages damage to open at the weak links within the microstructure, which are GBs with misorientations between 25 and 50 deg in this study, resulting in a larger fraction of disk-shaped voids from damage nucleating and preferentially growing along GBs. A quantitative analysis of the void shape distribution in several samples with varying thermomechanical histories is planned to expand upon the work presented here.

#### IV. CONCLUSIONS

To recap, 2-D statistics on GB misorientations with and without spall damage was obtained and analyzed on

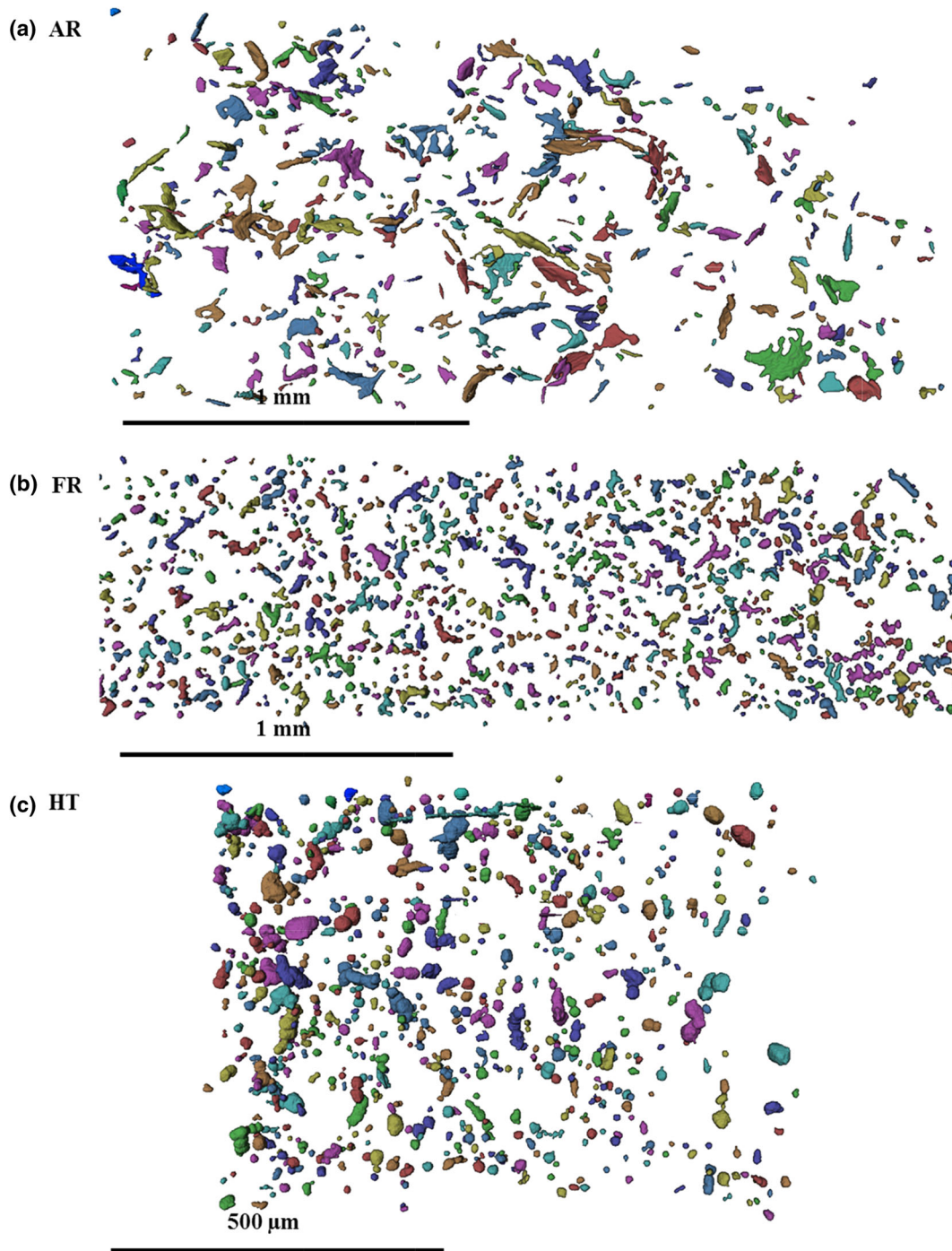


Fig. 6—3-D renderings of the spall planes in the three studied microstructures. Void colors are random and for visual aide only.

samples with three different thermomechanical histories, producing variations in grain size and plastic deformation. After normalizing the damaged boundaries with the global microstructure within the spall region to eliminate unwanted skewness of data from texture, it was found that random high-angle GBs with misorientations between 25 and 50 deg were favorable for having damage regardless of processing conditions. However, the preference for damage to nucleate within this

misorientation range was amplified when the sample contained plastic pre-strain, creating preference toward intergranular void nucleation and growth. It was found that low-angle GBs and  $\Sigma 3$  boundaries were resilient to void nucleation, with very few of them having damage despite the large quantity of  $\Sigma 3$ s found in all samples. The tips of terminated twins, which are likely not coherent, were, however, common sites for damage nucleation.



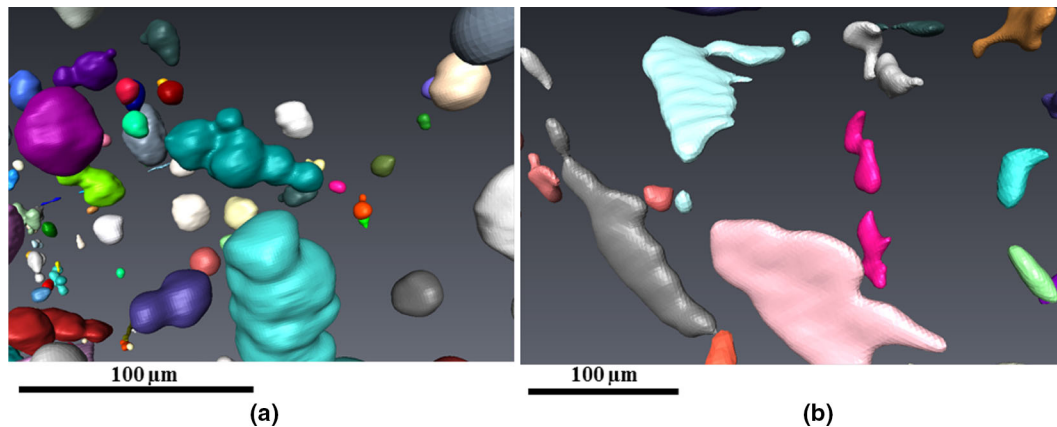


Fig. 7—Zoomed 3-D renderings of (a) coalesced and spherical voids in sample 6 (HT) and (b) intergranular sheet-like voids in sample 4 (AR). Void colors are random and for visual aid only.

3-D renderings of XRT data showed that there were vast differences in the void shapes in each microstructure. Plastically, pre-strained copper showed a large quantity of disk and needle-shaped voids, indicative of intergranular damage, including triple junctions and void coalescence. The annealed samples had a tendency for voids to be shaped as spheres and oblate and prolate ellipsoids, indicative of transgranular damage and coalescence, with the heaviest concentration of spherical voids coming from the microstructure containing the highest fraction of  $\Sigma 3$  boundaries. This strongly supports the conclusion reached from 2-D data that removal of plastic pre-strain allows damage nucleation to occur more randomly along the spall plane, with less preference to nucleate at GBs, but still maintaining a preference for the random high-angle 25 to 50 deg misorientation angle range when damage is nucleated or present at GBs. More work is needed to quantitatively link void shape distributions to the amount of inter- and transgranular damage present within the samples.

#### ACKNOWLEDGMENTS

This research work was funded by LANL under LDRD # 20060021DR, and by the Department of Energy, NNSA, under SSAA Grants # DE-FG52-06NA26169, DE-FG52-10NA29653., and DE-NA000 2005 and APS General User Proposal 35561. Eric Loomis, Pat Dickerson (LANL), Damian Swift (LLNL), David Wright, and Dallas Kingsbury (ASU) are thanked for their help during the various phases of the research work. Access to the TRIDENT Facility & Electron Microscopy Laboratory at LANL, Pavel Shevchenko at APS 2-BM, as well as the Center for High-Resolution Electron Microscopy and the Mechanical Testing Laboratory at ASU is gratefully acknowledged.

#### REFERENCES

1. D.R. Curran, L. Seaman, and D.A. Shockey: *Phys. Rep.*, 1897, vol. 147, pp. 253–388.
2. D.E. Grady: *J. Mech. Phys. Sol.*, 1988, vol. 36, pp. 353–84.
3. M.A. Meyers: *Dynamic Behavior of Materials*, Wiley, New York, 1994.
4. R. Vignjevic, N.K. Bourne, J.C.F. Millet, and T. De Vuyst: *J. Appl. Phys.*, 2002, vol. 92, pp. 4342–48.
5. R.W. Minich, J.U. Cazamias, M. Kumar, and A.J. Schwartz: *Metall. Mater. Trans. A*, 2004, vol. 35A, pp. 2663–73.
6. B.L. Henrie, T.A. Mason, and J.F. Bingert: in *Shock Compression of Condensed Matter 2005*, M.D. Furnish, M. Elert, T.P. Russell, and C.T. White, eds., American Institute of Physics, Melville, NT, 2005.
7. C. Czarnota, N. Jacques, S. Mercier, and A. Molinari: *J. Mech. Phys. Sol.*, 2008, vol. 56, pp. 1624–50.
8. P. Peralta, S. DiGiacomo, S. Hashemian, S.N. Luo, D. Paisley, R. Dickerson, E. Loomis, D. Byler, K.J. McClellan, and H.D'Armas: *Int. J. Damage*, 2009, vol. 18, pp. 393–413.
9. L. Wayne, K. Krishnan, S. DiGiacomo, N. Kovvali, P. Peralta, S.N. Luo, S. Greenfield, D. Byler, D. Paisley, K.J. McClellan, A. Koskelo, and R. Dickerson: *Scr. Mater.*, 2010, vol. 63, pp. 1065–68.
10. J.P. Escobedo, D. Dennis-Koller, E.K. Cerreta, B.M. Patterson, C.A. Bronkhorst, B.L. Hansen, D. Tonks, and R.A. Lebensohn: *J. Appl. Phys.*, 2011, vol. 110, p. 033513.
11. J.P. Escobedo, E.K. Cerreta, and D. Dennis-Koller: *JOM*, 2014, vol. 66, pp. 156–64.
12. A. Brown, K. Krishnan, L. Wayne, P. Peralta, S.N. Luo, D. Byler, and B. Patterson: *ASME IMECE*, San Diego, CA, 2013, p. 65642.
13. W. Han, Q. An, S.N. Luo, T. Germann, D. Tonks, and W. Goddard: *Phys. Rev. B*, 2012, vol. 85, p. 024107.
14. E.Q. Lin, H.J. Shi, L.S. Niu, and E.Z. Jin: *Comput. Mater. Sci.*, 2012, vol. 59, pp. 94–100.
15. S.J. Fensin, J.P. Escobedo, C. Brandl, E.K. Cerreta, G.T. Gray, III, T.C. Germann, and S.M. Valone: *Acta Mater.*, 2014, vol. 64, pp. 113–22.
16. J.F. Bingert, B.L. Henrie, and D.L. Worthington: *Metall. Mater. Trans. A*, 2007, vol. 38A, pp. 1712–21.
17. A.P. Sutton and R.W. Balluffi: *Interfaces in Crystalline Materials*, Oxford University Press, New York, 1995.
18. N.L. Johnson: *Biometrika*, 1949, vol. 36, pp. 149–76.
19. H.H. Ku: *J. Res. Natl. Bur. Stand.*, 1966, vol. 70C, pp. 263–73.
20. B.M. Patterson, J.P. Escobedo, D. Dennis-Koller, and E. Cerreta: *Microsc. Microanal.*, 2012, vol. 18, pp. 390–98.
21. A.L. Stevens, L. Davidson, and W.E. Warren: *J. Appl. Phys.*, 1972, vol. 43, pp. 4922–27.
22. V. Randle: *Interface Sci.*, 2002, vol. 10, pp. 271–77.
23. J.K. MacKenzie: *Biometrika*, 1958, vol. 45, pp. 229–40.
24. D.G. Brandon: *Acta Metall.*, 1966, vol. 14, pp. 1479–84.